Marfoua and Hong *NPG Asia Materials* (2024)16:6
https://doi.org/10.1038/s41427-023-00525-5

NPG Asia Materials

ARTICLE Open Access

Large anomalous transverse transport properties in atomically thin 2D Fe_3GaTe_2

Brahim Marfoua[1] and Jisang Hong[1]

Abstract

Anomalous transverse conductivities, such as anomalous Hall conductivity (AHC), anomalous Nernst conductivity (ANC), and anomalous thermal Hall conductivity (ATHC), play a crucial role in the emerging field of spintronics. Motivated by the recent fabrication of two-dimensional (2D) ferromagnetic thin film Fe_3GaTe_2, we investigate the thickness-dependent anomalous transverse conductivities of the 2D Fe_3GaTe_2 system (from one to four layers). The atomically ultrathin 2D Fe_3GaTe_2 system shows above-room-temperature ferromagnetism with a large perpendicular magnetic anisotropy energy. Furthermore, we obtain a large AHC of −485 S/cm in the four-layer thickness, and this is further enhanced to −550 S/cm with small electron doping. This AHC is seven times larger than the measured AHC in thicker 2D Fe_3GaTe_2 (178 nm). The ANC also reaches 0.55 A/K.m in the four-layer structure. Along with these, the four-layer system exhibits a large ATHC (−0.105 ~ −0.135 W/K.m). This ATHC is comparable to the large ATHC found in Weyl semimetal $Co_3Sn_2S_2$. Based on our results, the atomically ultrathin 2D Fe_3GaTe_2 system shows outstanding anomalous transverse conductivities and can be utilized as a potential platform for future spintronics and spin caloritronic device applications.

Introduction

Owing to their configurations and exceptional features for basic research and prospective industrial applications, two-dimensional (2D) materials have attracted extensive research interest and have triggered the curiosity of many researchers. To date, the fabrication of 2D magnetic materials are possible using advanced atomic manipulation techniques. Therefore, 2D ferromagnets and their magnetic ground states have caused intriguing issues: fabrication of atomically thin 2D magnetic materials and comprehension of magnetism in their 2D limit[1–3]. For example, layer-dependent ferromagnetism with out-of-plane anisotropy was found in CrI_3 and $Cr_2Ge_2Te_6$ flakes with semiconducting behavior[4,5]. However, these systems have low critical temperatures (<45 K). On the other hand, 2D VSe_2 was successfully grown from a bulk crystal with a 1 T phase[6,7]. Although the stability and phase issues of 2D VSe_2 are still under debate, room-temperature ferromagnetism was observed in the 1T-VSe_2 monolayer. Moreover, the 2D Fe_3GeTe_2 monolayer was also successfully synthesized with a critical temperature of ~130 K[8]. Notably, an ionic gating approach was used to create gate-tunable room-temperature ferromagnetism in four-layer Fe_3GeTe_2 flakes[9]. Therefore, 2D ferromagnet materials have potential in various multifunctional devices for potential spintronics applications, especially at room temperature.

In this regard, the exploration of 2D magnetic materials with a high Curie temperature (T_C) has been ongoing. For instance, based on the success of the 2D Fe_3GeTe_2, the 2D ferromagnetic crystal Fe_3GaTe_2 was also recently fabricated in thickness ranges from bulk down to 9.5 nm (~14 layer thickness). This 2D Fe_3GaTe_2 system showed a T_C of 350 ~ 380 K with large perpendicular magnetic anisotropy. This T_C was potentially record-high for known intrinsic 2D vdW ferromagnetic crystals[10]. However, anomalous Hall measurements and direct magnetic domain imaging were performed in the Fe_3GaTe_2 nanosheet thickness (178 nm) and not in the ultrathin

Correspondence: Jisang Hong (hongj@pknu.ac.kr)
[1]Department of Physics, Pukyong National University, Busan 48513, Korea

film structure. The maximum anomalous Hall conductivity in the nanosheet thickness (178 nm) was approximately 73 S/cm at low temperatures (~3 K) and was inversely proportional to the temperature. Moreover, the aforementioned anomalous Hall measurement was performed in the film thickness. Hence, the anomalous Hall properties in the ultrathin region or atomically thin (less than a few layer thickness) structures remain to be studied.

Moreover, the Berry phase and Berry curvature are key concepts in the study of condensed matter physics and are used to describe the geometric properties of a band structure in a periodic solid. This geometric information is related to anomalous transport properties such as the anomalous Hall effect (AHE), anomalous Nernst effect (ANE), and anomalous thermal Hall effect (ATHE) through anomalous off-diagonal coefficients. The interplay between the electron properties and the magnetic orders in magnetic materials is a central theme in the field of condensed matter physics due to its potential applications for high-density magnetic recording technologies: recording media, magnetic random access memory (MRAM), and magnetic sensors[11,12]. Berry-curvature-related quantities, such as the anomalous Hall conductivity (AHC), anomalous Nernst conductivity (ANC), and anomalous thermal Hall conductivity (ATHC), are strongly sensitive to the thickness in the 2D limit[13]. However, no studies on the anomalous off-diagonal response (AHE, ANE, and ATHE) in atomically thin (few layer thickness) 2D Fe_3GaTe_2 systems have been performed. Hence, in this study, we investigate the thickness-dependent magnetic properties (monolayer to four-layer thickness), anomalous transverse transport properties, magnetic anisotropy, and Curie temperature (T_C). Then, we show that 2D Fe_3GaTe_2 have better transverse transport properties than bulk or thicker systems.

Results

Thickness-dependent magnetic and electronic properties

Figure 1a–d shows the top and side views from the monolayer to the four-layer Fe_3GaTe_2 systems. The optimized lattice parameters are 4.04, 4.02, 4.00, and 4.02 Å for the monolayer, bilayer, trilayer, and four-layer systems, respectively. Note that the 2D Fe_3GaTe_2 system is experimentally fabricated. Therefore, we follow the same stacking order reported in the experimental study. These lattice parameters are similar to the reported value in the bulk system (3.98 Å)[10]. The interlayer distance in the bilayer, trilayer, and four-layer systems is approximately 2.90 Å, and the distance between the two central Fe atoms is 7.90 Å in each system. This result is also in good agreement with a previously reported value in the bulk system[10]. Then, we calculate the magnetic ground

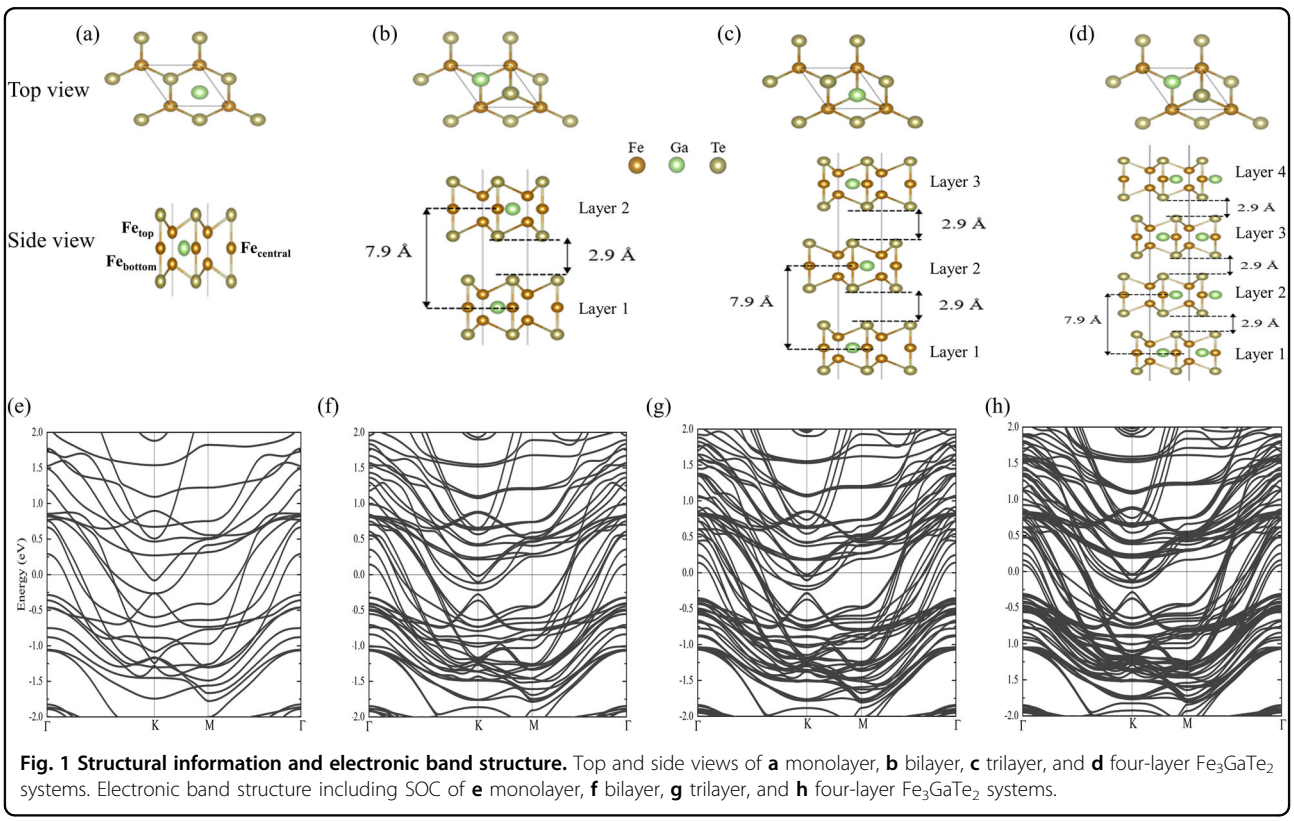

Fig. 1 Structural information and electronic band structure. Top and side views of **a** monolayer, **b** bilayer, **c** trilayer, and **d** four-layer Fe_3GaTe_2 systems. Electronic band structure including SOC of **e** monolayer, **f** bilayer, **g** trilayer, and **h** four-layer Fe_3GaTe_2 systems.

state by considering the total energy difference between the antiferromagnetic (AFM) and ferromagnetic (FM) states (E_{AFM}-E_{FM}). In the monolayer system, the total energy difference (ΔE_{ex}) is calculated by considering intralayer exchange coupling, and we find an energy difference ΔE_{ex} of 272 meV/unit-cell. Therefore, the monolayer structure shows the FM ground state. In the bilayer, trilayer, and four-layer systems, we consider both the intralayer and interlayer spin configurations. However, the intralayer AFM spin configuration is the most unstable state. Thus, we consider the layer-to-layer exchange coupling. In the bilayer system, the total energy difference, ΔE_{ex}, between the layer-to-layer FM and AFM states is 9 meV/unit-cell, while ΔE_{ex} becomes 20 meV/unit-cell and 34 meV/unit-cell in trilayer and four-layer structures. Overall, all the systems have an FM ground state. The monolayer system has a total magnetic moment of 5.87 μ_B/unit-cell, and this magnetic moment increased to 11.67 μ_B/unit-cell, 17.37 μ_B/unit-cell, and 23.25 μ_B/unit-cell in the bilayer, trilayer, and four-layer systems, respectively. Here, the Fe atom in the central sublayer ($Fe_{central}$) has a magnetic moment of 1.4 μ_B, while those of the top and bottom sublayers (Fe_{top} and Fe_{bottom}) have a magnetic moment of 2.3 μ_B. However, the magnetic moments of the Te and Ga atoms are approximately −0.1 μ_B, which are very small compared to that of the Fe atoms.

To further describe the magnetic properties of the 2D Fe_3GaTe_2 systems, we consider the Heisenberg model for the spins of the Fe atoms. Here, we use Green's function method, which treats the local rigid spin rotation as a perturbation[14]. In this case, the Heisenberg Hamiltonian can be expressed as follows:

$$H = -\sum_{ij} J_{ij}(m_i \cdot m_j) \quad (1)$$

where J_{ij} is the Heisenberg isotropic exchange, and m_i and m_j are the normalized magnetic moments. Here, we consider the pairs *I, j* with an extent up to the 3rd nearest neighbor (NN). Owing to the symmetry, we select four different intralayer spin pairs: Fe_{bottom}-Fe_{bottom} (equivalently Fe_{top}-Fe_{top}), $Fe_{central}$-$Fe_{central}$, Fe_{bottom}-$Fe_{central}$ (equivalently Fe_{top}-$Fe_{central}$), and Fe_{bottom}-Fe_{top} in the monolayer system. However, the bilayer, trilayer, and four-layer systems have both intralayer and interlayer exchange interactions. We select the layer 1 to layer 2 interaction in the bilayer and trilayer systems. Note that layer 1 and layer 3 have the same exchange interaction with layer 2 by symmetry in the trilayer system. Moreover, two interlayer interactions occur in the four-layer system owing to its symmetry: layer 1(4) to layer 2(3) and layer 3 to layer 2 interactions. We present the Heisenberg exchange constants J_{ij} up to the 3rd NN of the monolayer and bilayer systems in Tables 1 and 2. For the trilayer and four-layer systems, we present the results in the Supplementary Information (SI) Tables S1 and S2 with further discussion in Supplementary Note 1. Here, the positive exchange J values favor a ferromagnetic (FM) configuration, while the negative exchange J values indicate an antiferromagnetic (AFM) configuration.

Table 1 Calculated Heisenberg exchange (J) in meV using Green's function method of the Fe_3GaTe_2 monolayer.

Exchange interactions	J (1st NN) meV	J (2nd NN) meV	J (3rd NN) meV
Fe_{bottom}-Fe_{bottom} (Fe_{top}-Fe_{top})	2.03	−0.25	−0.42
$Fe_{central}$-$Fe_{central}$	−2.00	0.34	−1.28
Fe_{bottom}-Fe_{top}	75.15	−1.50	2.53
Fe_{bottom}-$Fe_{central}$ (Fe_{top}-$Fe_{central}$)	26.92	3.20	−1.50

Here, the 1st, 2nd, and 3rd nearest neighbor (NN) exchange interactions of the Fe atoms are provided.

Table 2 Calculated Heisenberg exchange (J) in meV using Green's function method of the Fe_3GaTe_2 bilayer.

Exchange interactions (intralayer)	J (1st NN) meV	J (2nd NN) meV	J (3rd NN) meV
Fe_{bottom}-Fe_{bottom} (Fe_{top}-Fe_{top})	−0.30	1.40	0.17
$Fe_{central}$-$Fe_{central}$	−1.10	0.31	−0.85
Fe_{bottom}-Fe_{top}	74.01	−0.15	0.75
Fe_{bottom}-$Fe_{central}$ (Fe_{top}-$Fe_{central}$)	27.03	1.25	−0.3
Fe_{top} (layer 1) - Fe_{bottom} (layer 2)	1.90	−0.38	−0.61
Fe_{top} (layer 1) - $Fe_{central}$ (layer 2)	0.82	0.68	−0.03
Fe_{top} (layer 1) - Fe_{top} (layer 2)	−0.77	−0.14	0.06

Here, the 1st, 2nd, and 3rd nearest neighbor (NN) exchange intralayer interactions of the Fe atoms (in layer 1) and the exchange interlayer interactions of the Fe atoms (layer 1–layer 2) are provided.

In the monolayer system, the 1st NN Fe_{bottom}-Fe_{bottom} interaction has J ~ 2 meV, favoring the FM configuration, and then decreases to J ~ −0.25 meV and −0.42 meV in the 2nd and 3rd NN interactions, respectively. The 1st NN $Fe_{central}$ - $Fe_{central}$ exchange interaction favors AFM coupling with a moderate strength of ~−2 meV, and this decreases to ~0.34 meV and −1.28 meV in the 2nd and 3rd NN interactions, respectively. The 1st NN Fe_{bottom}-Fe_{top} interaction has the largest exchange coupling of ~75 meV. This exchange coupling quickly drops in the 2nd and 3rd NN interactions, as indicated in Table 1. The 1st NN Fe_{bottom}-$Fe_{central}$ interaction has ~26 meV, with decreased values in the 2nd and 3rd NN interactions. Overall, the main exchange coupling is dominated by the 1st NN Fe_{bottom}-Fe_{top} interaction followed by the 1st NN Fe_{bottom}-$Fe_{central}$ interaction.

In the bilayer system, we find similar intralayer interactions as in the monolayer system. The main contribution is dominated by the 1st NN Fe_{bottom}-Fe_{top} exchange interactions with J ~74 meV and the 1st NN Fe_{bottom}-$Fe_{central}$ with J ~27 meV, favoring the FM configuration. Note that the exchange couplings quickly decrease in the

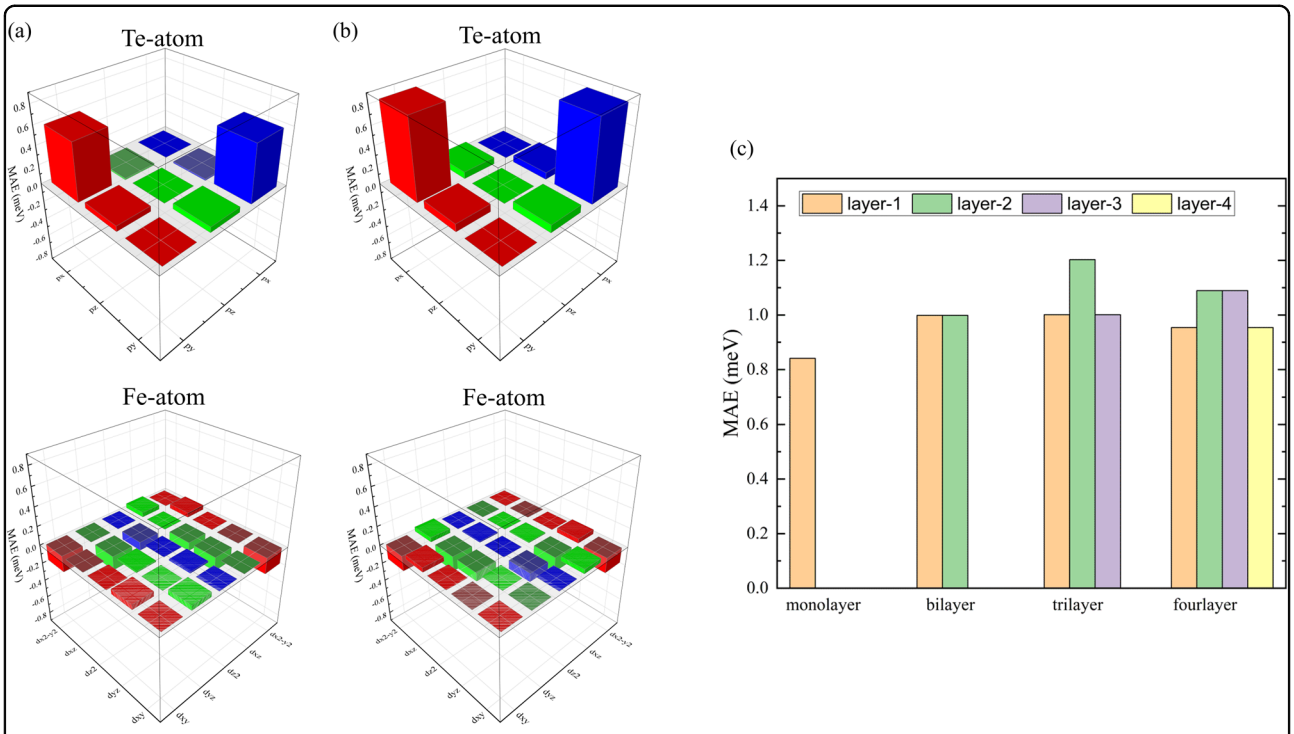

Fig. 2 SOC-resolved MAE. SOC-resolved MAE of the interface Te and Fe atoms in the **a** monolayer and **b** bilayer. **c** Layer-dependent magnetic anisotropy energy (MAE) of the monolayer, bilayer, trilayer, and four-layer Fe_3GaTe_2 systems.

2nd and 3rd NN interactions, as displayed in Table 2. However, the interlayer exchange interaction is rather weak compared with the intralayer interaction. The 1st NN Fe_{top} (layer 1) - Fe_{bottom} (layer 2) exchange interaction is only ~1.90 meV. Note that the trilayer and four-layer systems also favor the FM configuration (see Supplementary Note 1). In addition, we also calculate the exchange coupling between the Te and Fe atoms in the 2D Fe_3GaTe_2 system. The Fe-Te exchange coupling is very small compared with the Fe-Fe exchange coupling. For instance, the 1st NN exchange coupling strength in the monolayer system is ~1 meV, and this decreases to J~ 0.04 meV in the 2nd NN interaction. This result indicates that the influence of the Fe-Te exchange coupling on ferromagnetism is negligible. Figure 1e–h shows the thickness-dependent band structures in the FM state. In all systems, conventional metallic band structures are observed because both majority and minority spin bands cross the Fermi level. Note that the 2D thin Fe_3GaTe_2 system was reported as being metallic in a previous experimental report[10].

We also calculate the magnetic anisotropy, including the spin-orbit coupling (SOC). Here, the magnetic anisotropy energy (MAE) is obtained based on the total energy difference between the in-plane [001] and out-of-plane [100] magnetization directions. The monolayer system has an MAE of 0.59 meV/unit-cell, indicating perpendicular magnetic anisotropy. The perpendicular MAE is further increased to 1.89 meV/unit-cell, 3.28 meV/unit-cell, and 3.99 meV/unit-cell in the bilayer, trilayer, and four-layer systems, respectively. To understand this large perpendicular magnetic anisotropy, we further analyze the SOC matrix elements. Figure 2a, b shows the contributions to the magnetic anisotropy from the Fe and Te atoms of the monolayer and bilayer systems. For the trilayer and four-layer systems, we present the calculated results in Supplementary Information (SI) in Fig. S1(a)-(b). Note that no substantial contribution to the magnetic anisotropy from the Ga atoms is found. Here, a positive value indicates perpendicular magnetic anisotropy, while a negative value represents the in-plane contribution. The main contributions to the MAE originate from the Te element, followed by a relatively small contribution from the Fe element. In addition, the interface Te and Fe atoms are slightly more sensitive than the surface atoms. Hence, we present only the interface Te and Fe atoms as an illustration. As shown, the largest contribution to the perpendicular magnetic anisotropy originates from the SOC between $p_x - p_y$ orbitals, whereas the Fe atom has a rather small magnitude of the in-plane (negative) magnetic anisotropy through the SOC between d_{x2-y2} - d_{xy} orbitals and d_{xz} - d_{yz} orbitals. The MAE from the Te atom is ~0.6 meV in the monolayer and increases to ~0.80 meV in the bilayer system. However, the d_{x2-y2} - d_{xy} orbitals and d_{xz} - d_{yz} orbitals of the Fe atom have MAE contributions of −0.17 meV

and −0.14 meV in the monolayer, respectively, and these values become −0.16 meV in the bilayer system. Similar trends are found in both the trilayer and four-layer systems. Overall, the net magnetic anisotropy in all four systems is dominated by the Te atom and particularly the p_x - p_y orbitals. Moreover, the magnetic anisotropy is strongly sensitive to the orbital characteristics of the unoccupied and occupied states near the Fermi level because these states are correlated through SOC. In addition, the SOC strength is usually proportional to the atomic mass. Since the Te atom has a larger atomic mass than the Fe atom, the major contributions to the MAE originate from the Te atoms, although the Fe atoms dominate the magnetic moment. We also present the layer-dependent MAE to determine the evolution of the MAE on each layer. Figure 2c shows the MAE layer contribution of each system. In the bilayer system, each layer has the same contribution because both layers are in the same environment. However, the central layers have larger contributions to the MAE compared with the top and bottom layers in trilayer and four-layer systems.

The Curie temperature (T_C) is a key factor in determining the suitability of a ferromagnetic material for spintronic applications. Particularly, a material that has a T_C above room temperature is highly desirable. Thus, we calculate the thickness-dependent T_C of the 2D Fe_3GaTe_2 systems. We apply the Metropolis Monte Carlo (MC) simulation using the Heisenberg-type Hamiltonian. The Hamiltonian operator in the Heisenberg model with the magnetic anisotropy factor can be written as follows:

$$\hat{H} = -\sum_{i,j} J\hat{m}_i \cdot \hat{m}_j - k_2 \sum_i m_z^2 \tag{2}$$

where $\hat{m}_{i(j)}$ is the magnetic moment at sites i (j), and m_z is the spin aligned along a single easy axis. J and k_2 represent the exchange coupling parameter and the anisotropy constant, respectively. Note that the J values are evaluated based on Green's function method[14]. The anisotropy constant is estimated based on our calculated magnetic anisotropy energy (MAE). To calculate the temperature-dependent magnetization curve, we use a supercell of 50 × 50 for the monolayer system and 30 × 30 for the bilayer, trilayer, and four-layer systems using the VAMPIRE software package[15,16]. We employ 10000 equilibration steps and 10000 averaging steps. Figure 3a–d shows the temperature-dependent magnetization curves of the monolayer, bilayer, trilayer, and four-layer Fe_3GaTe_2 systems. Here, we fit the temperature-dependent magnetic curve using the Curie-Bloch equation as given below:

$$m(T) = \left[1 - \frac{T}{T_C}\right]^{\beta} \tag{3}$$

The monolayer system has a T_C of 310 K, which is further increased to 340 K, 358 K, and 374 K in the bilayer, trilayer, and four-layer systems, respectively. This enhancement of the T_C as a function of thickness is due to the introduction and enhancement of the interlayer exchange along with the intralayer exchange from the monolayer to the four-layer systems. Note that the layer-to-layer exchange is enhanced with increasing thickness from the bilayer to the four-layer thickness in the 2D Fe_3GaTe_2 systems, and this leads to the enhancement of the T_C up to the four-layer system. Overall, the calculated Curie temperatures of the atomically thin 2D Fe_3GaTe_2 systems are similar to those of the T_C in relatively thicker 2D Fe_3GaTe_2 (350 ~ 380 K) and bulk systems (365 K)[10]. The 2D Fe_3GaTe_2 shows a much larger T_C than the 2D Fe_3GeTe_2 monolayer (~130 K)[8]. Moreover, we investigate the effect of magnetic shape anisotropy on T_C. Thus, we calculate the critical temperature assuming in-plane anisotropy, and the calculated T_C is presented in SI Fig. S2. The calculated T_C with in-plane anisotropy slightly decreases by only 1–5 K in all 2D Fe_3GaTe_2 systems (from mono- to four-layer) in comparison to the T_C calculated with out-of-plane anisotropy. This result indicates the negligible effect of magnetic shape anisotropy on the critical temperature.

Thickness-dependent anomalous transport coefficients

Onsager's generalized transport equations (Onsager's reciprocal relations) relate the transport coefficients to the thermodynamic forces and fluxes in a system. For the off-diagonal transport coefficients, Onsager's generalized transport equations can be expressed as follows:

$$\begin{pmatrix} J \\ Q \end{pmatrix} = \begin{pmatrix} l_{11} & l_{12} \\ l_{21} & l_{22} \end{pmatrix} \begin{pmatrix} E \\ \nabla T \end{pmatrix} \tag{4}$$

where J and Q are the charge current density and the heat current density, respectively, while E and ∇T are the electric field and applied temperature gradient, respectively. Note that we consider the intrinsic anomalous transport coefficients to originate from an anomalous velocity that produces the intrinsic (Karplus–Luttinger) mechanism in terms of Berry curvature. Thus, the l_{11} component represents the AHC. At zero temperature, the AHC (σ_{xy}) can be obtained from the Kubo formula and Berry phase theory by integrating the Berry curvature over the whole Brillouin zone (BZ)[17,18]:

$$l_{11} = \sigma_{xy} = \frac{e^2}{\hbar} \int_{BZ} \frac{d^3k}{(2\pi)^3} \Omega(k) \tag{5}$$

where the Berry curvature $\Omega(k)$ is given by the following:

$$\Omega(k) = \sum_n f_n \Omega_n(k) \tag{6}$$

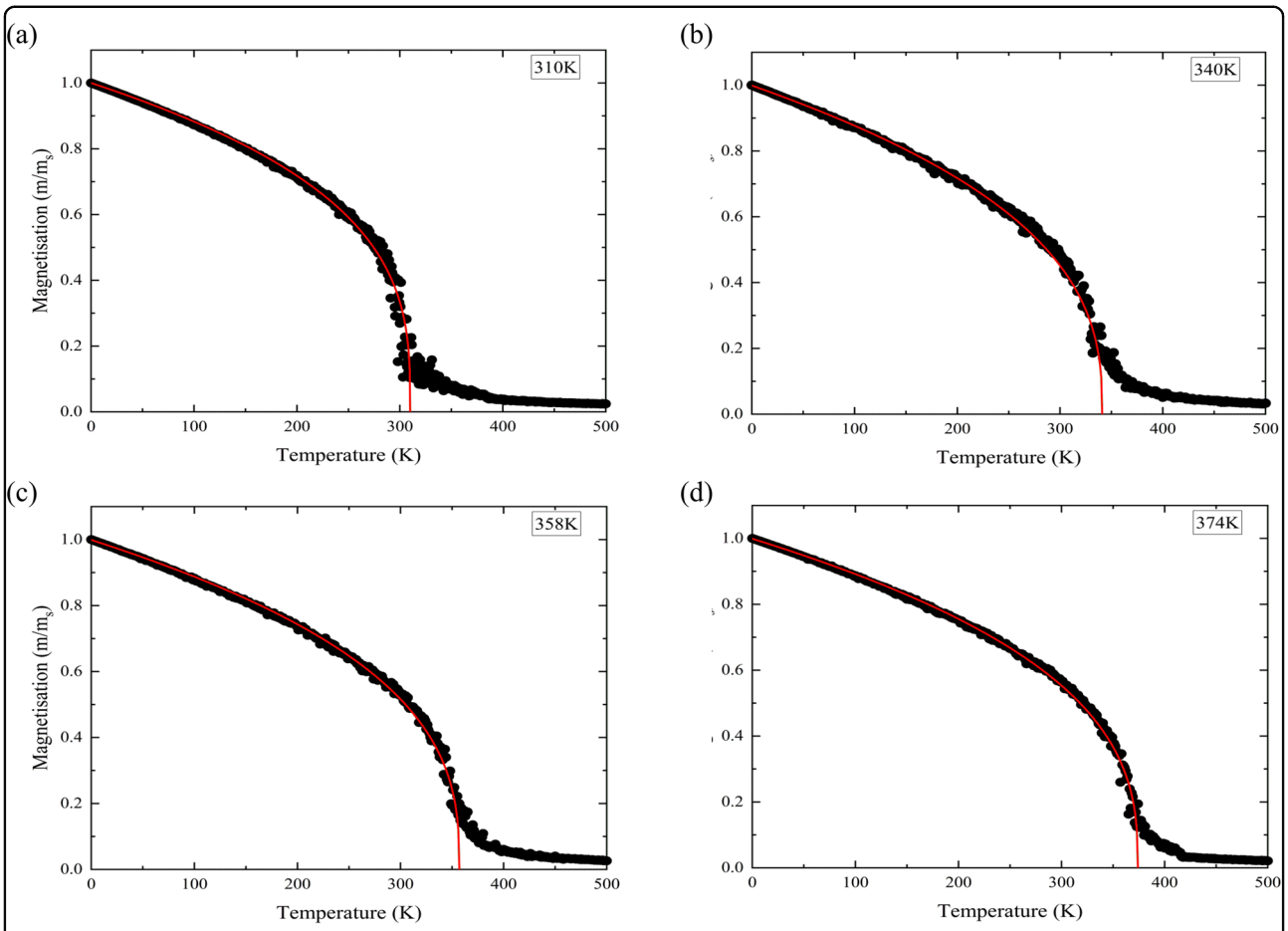

Fig. 3 Monte Carlo simulation for the magnetization. Temperature-dependent magnetization curve of the **a** monolayer, **b** bilayer, **c** trilayer, and **d** four-layer Fe_3GaTe_2 systems. Here, the calculated T_C is 300 K, 325 K, 340 K, and 352 K in the monolayer, bilayer, trilayer, and four-layer systems, respectively.

$$\Omega_n(k) = -2Im\sum_{m\neq n}\frac{\langle u_{nk}|v_x|u_{mk}\rangle\langle u_{mk}|v_y|u_{nk}\rangle}{(E_{mk}-E_{nk})^2} \quad (7)$$

where f_n, $v_{x,y}$, and u_{nk} represent the Fermi-Dirac distribution function, velocity operator, and periodic part of the Bloch wave function with eigenvalue E_{nk}, respectively. Based on the well-constructed maximize localized Wannier functions (MLWFs), the projected Bloch wave functions (density functional theory Hamiltonian) onto high symmetry Wannier functions are used to calculate the Fourier transformed Wannier Hamiltonian. Figure 4 shows the calculated thickness-dependent AHC as a function of the chemical potential of the monolayer, bilayer, trilayer, and four-layer systems. The magnitude of the AHC increases with film thickness. For instance, the four-layer thickness structure has an AHC of -485 S/cm at zero chemical potential (μ). By varying the chemical potential, the AHC increases with electron doping, while the reverse behavior is obtained with hole doping. In particular, the maximum magnitude of the AHC in the four-layer system is approximately −550 S/cm at a 40 meV chemical potential. Note that the chemical potential of 40 meV can be considered minor because it is almost half an order of magnitude smaller than that considered in 2D $FeCl_2$[19], and the maximum AHC in the four-layer system is almost 1.5 times larger than that found in 2D $FeCl_2$. For comparison, we present both AHC (red line) and AHC per layer (black line) at zero chemical potential of the monolayer, bilayer, trilayer, and four-layer systems with an experimental measurement of AHC at 220-layer thickness Fe_3GaTe_2 (~178 nm)[10] in Fig. 5a. To be consistent, we show the absolute AHC ($|\sigma_{xy}|$) at zero carrier doping. The AHC in the monolayer system is approximately 165 S/cm and slightly increases to 185 S/cm in the bilayer. However, the AHC is substantially increased to 275 S/cm and 485 S/cm in the trilayer

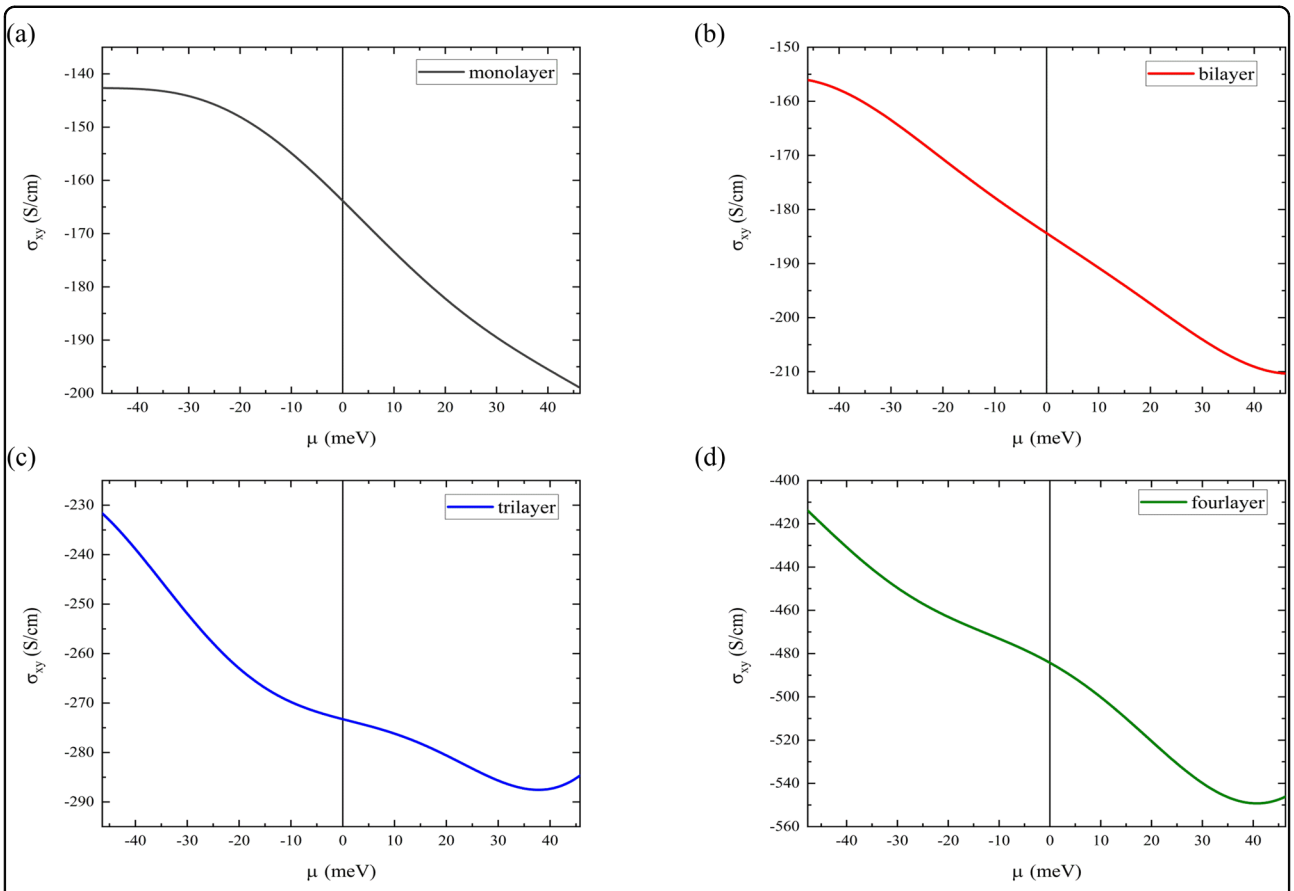

Fig. 4 Thickness-dependent anomalous Hall conductivity. Calculated anomalous Hall conductivity (σ_{xy}) as a function of the chemical potential of **a** monolayer, **b** bilayer, **c** trilayer, and **d** four-layer Fe_3GaTe_2 systems.

and four-layer systems, respectively. Note that the magnitude of the experimentally measured AHC of the 220-layer thickness system is approximately 73 S/cm at 3 K. Therefore, the ultrathin Fe_3GaTe_2 films with at least a four-layer thickness have larger values than those found in the thick film structure. In particular, the four-layer structure has an almost seven times larger AHC than the thick film structure. Additionally, the four-layer system shows a larger AHC than the thin film Fe_3GeTe_2 system (360 S/cm)[20]. Note that the variation in the AHC is caused by its sensitivity to the Berry curvature, which will be discussed later. On the other hand, the AHC values per layer show different behaviors. The AHC of the monolayer is ~165 S/cm, as indicated by the black color in Fig. 5a. However, with increasing thickness, the contribution to the AHC per layer is in the range of ~80–120 S/cm. The AHC per layer in ultrathin 2D Fe_3GaTe_2 (mono- to four-layer) is larger than that measured in the thick Fe_3GaTe_2 system (AHC per layer ~0.33 S/cm)[10]. We attribute this behavior to the quantum confinement effects in low-dimensional systems.

On the other hand, ANC (α_{xy}) can be expressed as follows[21]:

$$l_{12} = \alpha_{xy} = \frac{1}{eT}\int d\varepsilon\,(\varepsilon - \mu)\frac{\partial f}{\partial \varepsilon}\sigma_{xy} \tag{8}$$

where e, μ, and f are the elementary positive charge, chemical potential, and Fermi-Dirac distribution function, respectively. Figure 5b shows the thickness-dependent ANC as a function of the chemical potential at 100 K by applying the Mott relation[21]. At zero chemical potential, the monolayer has an ANC of 0.23 A/K.m, with a slight decrease to 0.15 A/K.m in the bilayer system, and it is approximately 0.05 A/K.m in the trilayer structure. However, the ANC in the four-layer has 0.32 A/K.m. at zero chemical potential. Moreover, the ANC is not enhanced with either electron or hole doping in the monolayer and bilayer systems. However, the ANC can be manipulated by small carrier doping in the trilayer and four-layer systems. For instance, the trilayer system exhibits a maximum ANC of −0.35 A/K.m at a chemical potential of −35 meV, and the ANC is further increased to 0.55 A/K.m in the four-layer system at −45 meV. Furthermore, the ANC in the

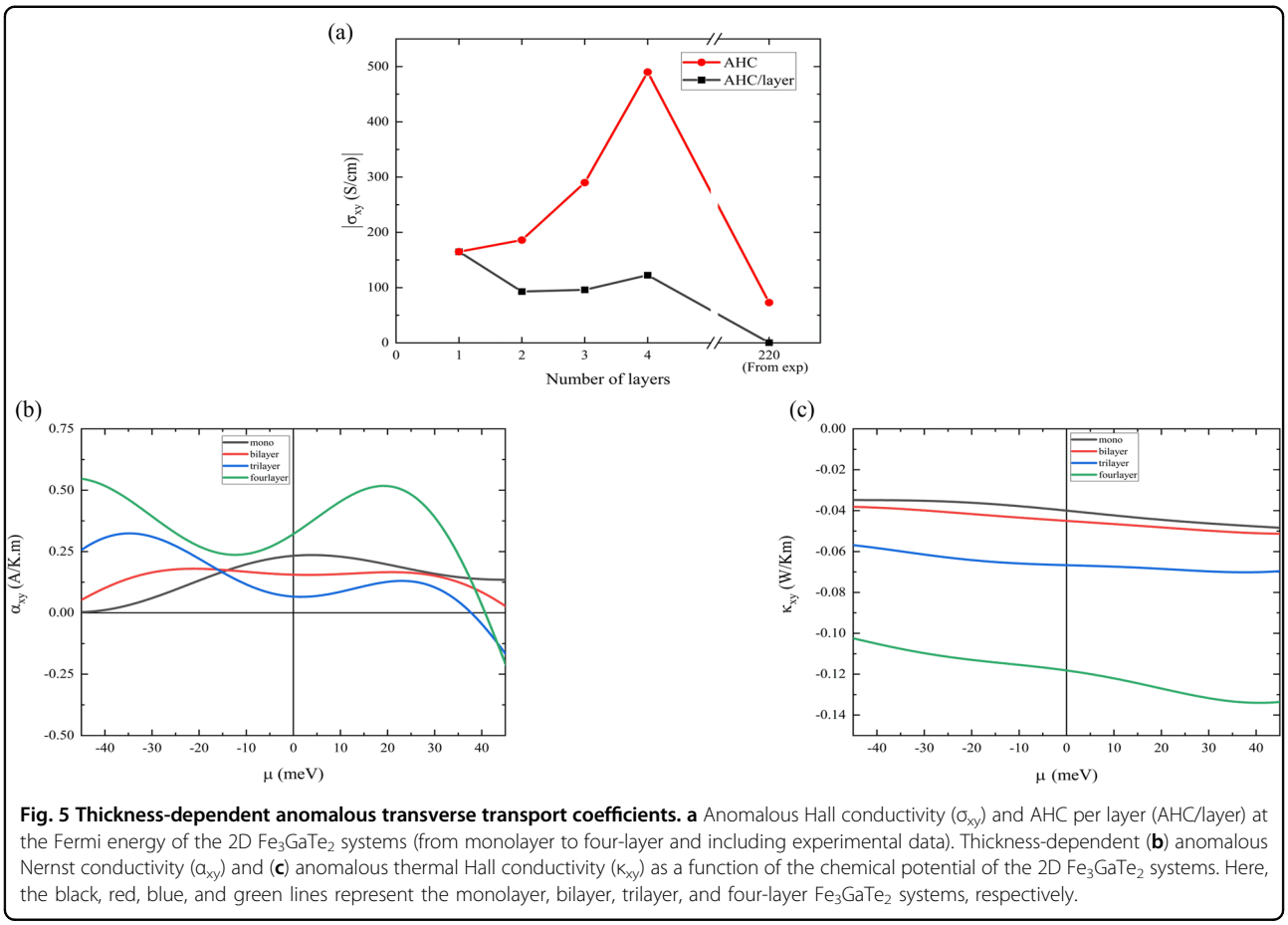

Fig. 5 Thickness-dependent anomalous transverse transport coefficients. a Anomalous Hall conductivity (σ_{xy}) and AHC per layer (AHC/layer) at the Fermi energy of the 2D Fe_3GaTe_2 systems (from monolayer to four-layer and including experimental data). Thickness-dependent (**b**) anomalous Nernst conductivity (α_{xy}) and (**c**) anomalous thermal Hall conductivity (κ_{xy}) as a function of the chemical potential of the 2D Fe_3GaTe_2 systems. Here, the black, red, blue, and green lines represent the monolayer, bilayer, trilayer, and four-layer Fe_3GaTe_2 systems, respectively.

four-layer structure is slightly larger than those found in other 2D materials, such as 2D Fe_3GeTe_2 (0.3 A/K.m at 130 K)[20] and 2D $FeCl_2$ (0.3 ~ 0.4 A/K.m at 100 K)[19]. We also calculate the Nernst thermopower (S_{xy}) of the 2D Fe_3GaTe_2 systems, and they are shown in SI Fig. S3. Note that further details can be found in Supplementary Note 2. The Nernst thermopower is ~−0.32 μV/K to 1 μV/K at zero chemical potential, which is lower than that of ferromagnetic $Co_3Sn_2S_2$ (~3 μV/K) at 80 K[22]. However, these Nernst thermopower (S_{xy}) values can be largely increased by either hole or electron doping. In particular, the largest maximum Nernst thermopower of $S_{xy} \sim 7.5$ μV/K is obtained in the monolayer system with hole doping (μ ~ 0.34 meV).

We also calculate the anomalous thermal Hall conductivity (ATHC), which represents the transverse thermal current induced by a longitudinal gradient of temperature. The ATHC can be written according to the linear response relation[11]:

$$l_{22} = \kappa_{xy} = \frac{1}{\hbar T}\int d\varepsilon\left(-(\varepsilon-\mu)^2\frac{\partial f}{\partial \varepsilon}\right)\sigma_{xy} \quad (9)$$

Note that the AHC and ATHC can be correlated with each other using the Wiedemann-Franz (WF) law and based on the anomalous Lorenz ratio, which is defined as follows:

$$\kappa_{xy} = L_{xy}\sigma_{xy}T \quad (10)$$

where L_{xy} is the anomalous Lorenz ratio, which is a constant ratio of ~2.44×10^{-8} Ω.W/K^2. Figure 5c shows the thickness-dependent ATHC as a function of the chemical potential at 100 K. Evidently, the spectral shape of the ATHC is similar to that of the AHC due to its correlation. At zero chemical potential, the ATHC is approximately −0.04 W/K.m, −0.045 W/K.m, −0.065 W/K.m, and −0.105 W/K.m in the monolayer, bilayer, trilayer, and four-layer systems, respectively. In particular, the ATHC of the four-layer system is similar to the reported large ATHC in the Weyl semimetal $Co_3Sn_2S_2$ (~0.14 W/K.m) at 80 K[23] and larger than that of the 2D Fe_3GeTe_2 system (0.04–0.11 W/K.m) at 130 K[24]. Note that this can be further increased up to −0.135 W/K.m with small electron doping (chemical potential of 40 meV).

Thickness-dependent distribution of Berry curvature

All anomalous transverse transport coefficients are correlated with each other according to Onsager's generalized transport equations. From a fundamental point of view, all transverse transport quantities are related to the AHC, and this AHC can be obtained from the Berry curvatures. For instance, the AHC is determined by the integration of the total Berry curvature of the occupied states at each k point in the whole Brillouin zone (BZ). Hence, as an illustration, we calculate the momentum resolved of the Berry curvature over the 2D plane (k_x, k_y) at the Fermi energy (zero chemical potential) to interpret the variation in the thickness dependent AHC behavior. Notably, the electronic structure is strongly sensitive to the film thickness in atomically thin structures, which affects the Berry curvature along with the structural symmetric feature. Figure 6a–d shows the distribution of the Berry curvature in the reciprocal space for monolayer, bilayer, trilayer, and four-layer systems. The boundary lines are indicated by black solid lines with Γ, M, K, and K$^-$ points. Note that the blue color indicates a positive Berry contribution, while the red color represents a negative contribution. A positive value of the Berry curvature leads to a positive AHC magnitude and vice versa. Note that the odd number of layers in the 2D Fe_3GaTe_2 system belongs to the subgroup of D3h-1 (187 space group). It has both 3-fold symmetry and a broken inversion symmetry along with the lack of the additional three vertical mirror planes of the full D3h point group. In the monolayer system, due to the broken inversion symmetry, the Berry curvature contributions from K corners cancel each other and disappear. The small positive Berry curvatures originate near the Γ point, but more pronounced negative Berry curvatures are found by the many general k-points, and these contributions are accumulated. This results in a net negative AHC. Different from the odd number of layers structure, the even number of layers structure belongs to the subgroup of the D3d-3 point group (164 space group), which has a total of 6 symmetry operations, including the inversion symmetry. Therefore, in the bilayer structure, the K corners show the same Berry curvature contributions (with small positive contributions). Moreover, small

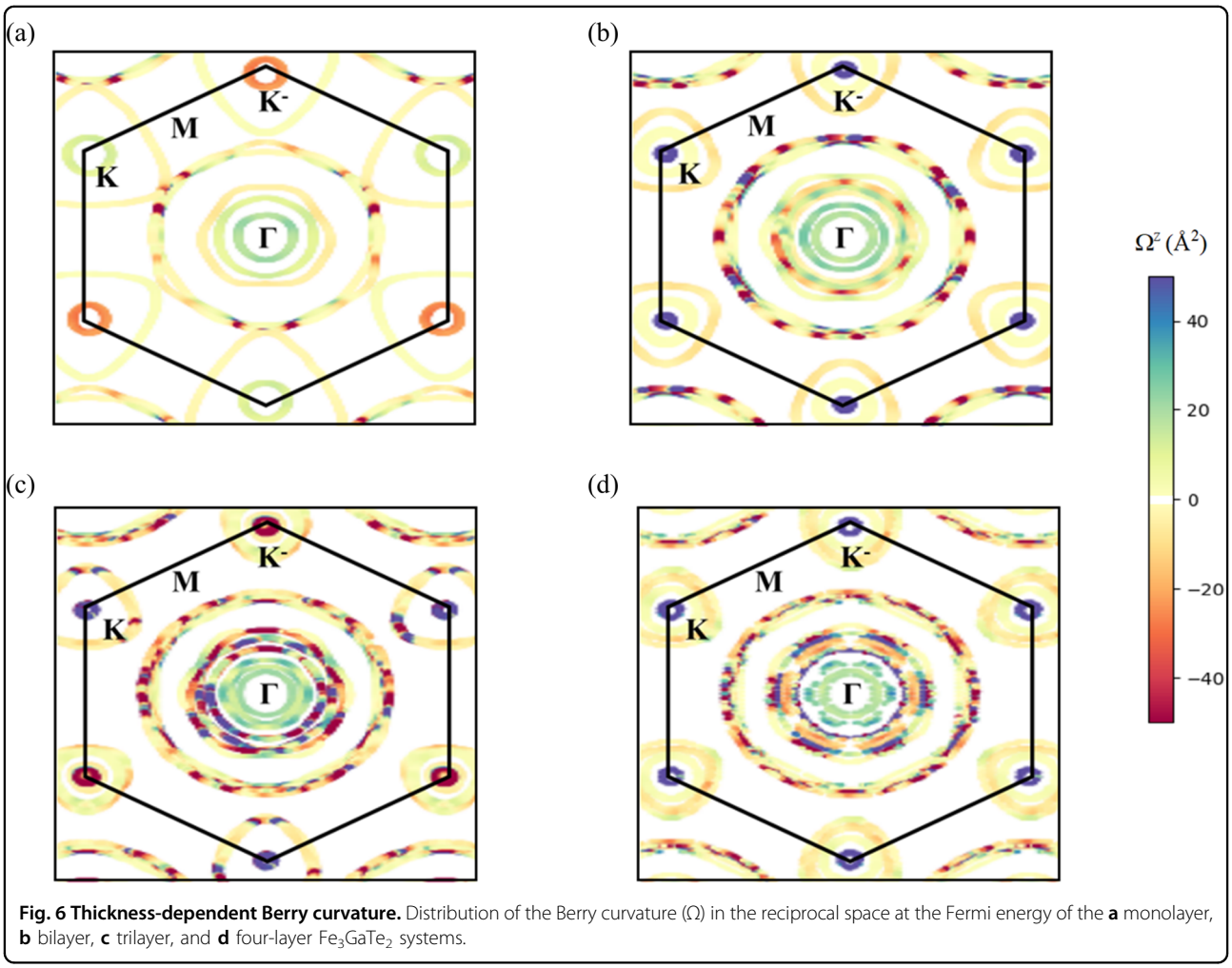

Fig. 6 Thickness-dependent Berry curvature. Distribution of the Berry curvature (Ω) in the reciprocal space at the Fermi energy of the **a** monolayer, **b** bilayer, **c** trilayer, and **d** four-layer Fe_3GaTe_2 systems.

positive Berry contributions are also present near the Γ point. However, the negative Berry curvature contributions are more dominant along the general k-points. These negative Berry curvature contributions accumulated, which results in a negative AHC in the bilayer system. In the trilayer system, we find similar behavior near the K corners as in the monolayer structure since it also has an odd number of layers. Additionally, small positive Berry contributions appear near the Γ point. However, greater dominance of the negative Berry contributions over the positive ones from the general k-points are observed. Thus, the negative AHC in the trilayer system is increased compared to those of the monolayer and bilayer systems. In the four-layer system, the Berry curvatures at the K corners show almost the same behavior as in the bilayer system due to the same symmetry. Additionally, small positive Berry curvatures are found around the Γ point. Nonetheless, the negative Berry curvatures along the general k-points are more dominant, and their magnitudes are larger than the positive ones. Consequently, this results in a larger negative AHC in the four-layer system. Overall, no single dominating contribution to the Berry curvature contribution appears from a particular k-point; however, all negative Berry contributions are accumulated from general k-points compared to the positive ones. Note that the behavior of ANC and ATHC properties are linked to the AHC features.

Discussion

In summary, we explore the thickness-dependent magnetic properties of the 2D Fe_3GaTe_2 system. The monolayer system has a T_C of 300 K, which is further increased to 325 K, 340 K, and 352 K in the bilayer, trilayer, and four-layer systems. We attain the perpendicular magnetic anisotropy from the monolayer to the four-layer thickness. The MAE energy increases with thickness. The perpendicular magnetic anisotropy originates from the SOC coupling of the Te atom, whereas the Fe contribution is quite weak. Similar to the magnetic anisotropy, the AHC also increases with increasing film thickness up to a four-layer thickness. For instance, the four-layer thickness structure has an AHC of −485 S/cm at zero chemical potential, and this can be enhanced to -550 S/cm with small electron doping. Based on the analysis of the momentum resolved from the Berry curvature, the AHC magnitude is mainly related to the accumulation of negative Berry curvature from general k-points and not from a single special k-point. The ANC of the four-layer system is 0.32 A/K.m at zero chemical potential. The magnitude of ANC can be further increased to 0.55 A/K.m with small hole doping. The Nernst thermopower (S_{xy}) is also calculated, and the largest maximum Nernst thermopower of $S_{xy} \sim 7.5$ μV/K can be obtained in the monolayer system with hole doping. In addition, the ATHC reaches approximately −0.105 W/K.m in the four-layer system and can be further enhanced to −0.135 W/K.m with electron doping. Overall, the 2D ultrathin Fe_3GaTe_2 system shows room-temperature ferromagnetism incorporating outstanding transverse transport properties. In particular, the four-layer system shows superior transverse transport properties. Our findings potentially indicate that the atomically thin 2D Fe_3GaTe_2 can be utilized for potential spintronics and spin caloritronic device applications.

Methods

First-principles calculations

We perform first-principles calculations using the Vienna ab initio simulation package (VASP)[25,26] with a projector augmented wave (PAW) set[26,27] and the Perdew-Burke-Ernzerhof (PBE) exchange correlational functional with generalized gradient approximation (GGA)[28]. Note that the PBE-GGA is demonstrated to appropriately address the exchange and correlation effects, and the results are in agreement with experimental measurements[10]. The energy cutoff of the plane wave is set to 650 eV, and the energy criterion is set to 10^{-6} eV with the forces less than 0.02 eV/Å on all relaxed structures. The Brillouin zone is sampled on a k-mesh of 19 × 19 × 1, and a vacuum distance of 20 Å is used to prevent artificial interactions along the z-direction. The van der Waals (vdW) interaction is included using the Grimme DFT-D3 method[29], and spin-orbit coupling (SOC) is also considered in the noncollinear calculations.

Magnetic anisotropy, magnetic interactions, and Curie temperature calculations

The magnetic anisotropy energy is calculated as the total energy difference between the in-plane [001] and out-of-plane [100] magnetization directions. Since the magnetic anisotropy requires more accurate k-mesh points, we carefully check the energy convergence up to 21 × 21 k-mesh. The exchange magnetic interaction parameters are calculated using Green's function method based on magnetic force theory (MFT) as implemented in the TB2J code[14]. The Curie temperature is estimated using Metropolis Monte Carlo simulations implemented in the VAMPIRE software package[15,16].

Wannier function (WF) calculations

The calculation of the Berry curvature and anomalous Hall conductivity is handled based on the Wannier functions, which are extracted from the band structure using the maximally localized Wannier function method[30]. Here, a finer k-mesh of 300 × 300 × 1 is used to accurately construct real-space Wannier functions for the calculation of the transverse electric response properties using a tight-binding Hamiltonian.

Acknowledgements
This work was supported by the National Research Foundation of Korea (NRF) grant funded by the Korean government (MSIT) (2022R1A2C1004440) and by the Supercomputing Center/Korea Institute of Science and Technology Information with supercomputing resources including technical support (KSC-2023-CRE-0190).

Author contributions
J.H. conceived the idea of this study. B.M. performed DFT calculations. J.H. and B.M. wrote and revised the manuscript.

Data availability
The data that support the findings of this study are available from the corresponding author upon reasonable request.

Code availability
The codes that support the findings of this study are available from the corresponding author upon reasonable request.

Competing interests
The authors declare no competing interests.

Publisher's note
Springer Nature remains neutral with regard to jurisdictional claims in published maps and institutional affiliations.

Supplementary information The online version contains supplementary material available at https://doi.org/10.1038/s41427-023-00525-5.

Received: 9 June 2023 Revised: 3 November 2023 Accepted: 7 November 2023
Published online: 26 January 2024

References

1. Gibertini, M., Koperski, M., Morpurgo, A. F. & Novoselov, K. S. Magnetic 2D materials and heterostructures. *Nat. Nanotechnol.* **14**, 408–419 (2019).
2. O'Hara, D. J. et al. Room temperature intrinsic ferromagnetism in epitaxial manganese selenide films in the monolayer limit. *Nano Lett.* **18**, 3125–3131 (2018).
3. Burch, K. S., Mandrus, D. & Park, J. G. Magnetism in two-dimensional van der Waals materials. *Nature* **563**, 47–52 (2018).
4. Huang, B. et al. Layer-dependent ferromagnetism in a van der Waals crystal down to the monolayer limit. *Nature* **546**, 270 (2017).
5. Gong, C. et al. Discovery of intrinsic ferromagnetism in two-dimensional van der Waals crystals. *Nature* **546**, 265 (2017).
6. Bonilla, M. et al. Strong room-temperature ferromagnetism in VSe 2 monolayers on van der Waals substrates. *Nat. Nanotechnol.* **13**, 289 (2018).
7. Yu, W. et al. Chemically exfoliated VSe2 monolayers with room-temperature ferromagnetism. *Adv. Mater.* **31**, 1903779 (2019).
8. Fei, Z. et al. Two-dimensional itinerant ferromagnetism in atomically thin Fe_3GeTe_2. *Nat. Mater.* **17**, 778 (2018).
9. Deng, Y. et al. Gate-tunable room-temperature ferromagnetism in two-dimensional Fe_3GeTe_2. *Nature* **563**, 94–99 (2018).
10. Zhang, G. et al. Above-room-temperature strong intrinsic ferromagnetism in 2D van der Waals Fe_3GaTe_2 with large perpendicular magnetic anisotropy. *Nat. Commun.* **13**, 1–8 (2022).
11. Xu, L. et al. Finite-temperature violation of the anomalous transverse Wiedemann-Franz law. *Sci. Adv.* **6**, eaaz3522 (2020).
12. Sharma, G., Goswami, P. & Tewari, S. Nernst and magnetothermal conductivity in a lattice model of Weyl fermions. *Phys. Rev. B* **93**, 035116 (2016).
13. Culcer, D., Keser, A. C., Li, Y. & Tkachov, G. Transport in two-dimensional topological materials: recent developments in experiment and theory. *2D Mater.* **7**, 022007 (2020).
14. He, X., Helbig, N., Verstraete, M. J. & Bousquet, E. TB2J: A python package for computing magnetic interaction parameters. *Comput. Phys. Commun.* **264**, 107938 (2021).
15. Evans, R. F. et al. Atomistic spin model simulations of magnetic nanomaterials. *J. Phys.: Condens. Matter* **26**, 103202 (2014).
16. Evans, R. VAMPIRE software package version 4.0, York, UK. https://vampire.york.ac.uk/ (2016).
17. Wang, X., Yates, J. R., Souza, I. & Vanderbilt, D. Ab initio calculation of the anomalous Hall conductivity by Wannier interpolation. *Phys. Rev. B* **74**, 195118 (2006).
18. Cai, T. et al. Magnetic control of the valley degree of freedom of massive Dirac fermions with application to transition metal dichalcogenides. *Phys. Rev. B* **88**, 115140 (2013).
19. Syariati, R., Minami, S., Sawahata, H. & Ishii, F. First-principles study of anomalous Nernst effect in half-metallic iron dichloride monolayer. *APL Mater.* **8**, 041105 (2020).
20. Xu, J., Phelan, W. A. & Chien, C. L. Large anomalous Nernst effect in a van der Waals ferromagnet Fe3GeTe2. *Nano Lett.* **19**, 8250–8254 (2019).
21. Xiao, D., Yao, Y., Fang, Z. & Niu, Q. Berry-phase effect in anomalous thermoelectric transport. *Phys. Rev. Lett.* **97**, 026603 (2006).
22. Guin, S. N. et al. Zero-Field Nernst Effect in a Ferromagnetic Kagome-Lattice Weyl-Semimetal $Co_3Sn_2S_2$. *Adv. Mater.* **31**, 1806622 (2019).
23. Karmakar, A. R., Nandy, S., Taraphder, A. & Das, G. Giant anomalous thermal Hall effect in tilted type-I magnetic Weyl semimetal $Co_3Sn_2S_2$. *Phys. Rev. B* **106**, 245133 (2022).
24. Yang, X., Zhou, X., Feng, W. & Yao, Y. Strong magneto-optical effect and anomalous transport in the two-dimensional van der Waals magnets $Fen-GeTe_2$ (n= 3, 4, 5). *Phys. Rev. B* **104**, 104427 (2021).
25. Kresse, G. & Furthmüller, J. Efficient iterative schemes for ab initio total-energy calculations using a plane-wave basis set. *Phys. Rev. B* **54**, 11169 (1996).
26. Kresse, G. & Joubert, D. From ultrasoft pseudopotentials to the projector augmented-wave method. *Phys. Rev. B* **59**, 1758 (1999).
27. Blochl, P. Projector augmented-wave method. *Phys. Rev. B* **50**, 17953 (1994).
28. Perdew, J. P., Burke, K. & Ernzerhof, M. Generalized gradient approximation made simple. *Phys. Rev. Lett.* **77**, 3865 (1996).
29. Grimme, S., Antony, J., Ehrlich, S. & Krieg, H. A consistent and accurate ab initio parametrization of density functional dispersion correction (DFT-D) for the 94 elements H-Pu. *J. Chem. Phys.* **132**, 154104 (2010).
30. Pizzi, G. et al. Wannier90 as a community code: new features and applications. *J. Phys.: Condens. Matter* **32**, 165902 (2020).